ACS NANO

www.acsnano.org

ARTICLE

Nonvolatile Transition of Molecular Orbital Gating for Reconfigurable Molecular Ambipolar Transistor Switch

Jung Sun Eo,[▽] Takgyeong Jeon,[▽] Young Ran Park, Hyeon Bin Kim, Eunyoung Lee, Sukang Bae, Hyunhak Jeong, Takhee Lee, and Gunuk Wang*

Cite This: *ACS Nano* 2025, 19, 41386–41395

Read Online

ACCESS | Metrics & More | Article Recommendations | Supporting Information

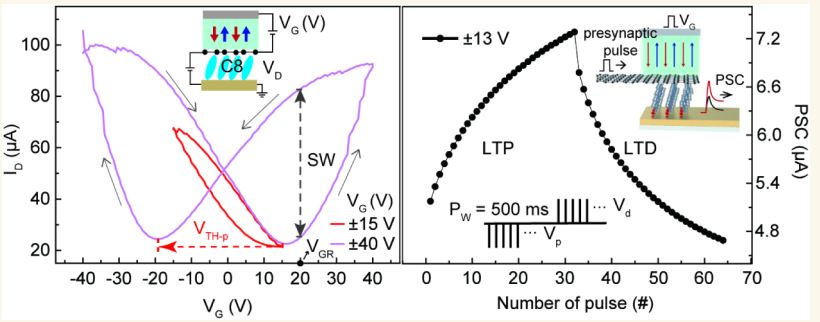

ABSTRACT: **Molecular electronics offers a promising avenue for ultimate device miniaturization, yet realizing versatile functionalities such as nonvolatile ambipolar switching in a robust solid-state transistor platform. Here, we report a reconfigurable molecular transistor switch achieved by vertically integrating an alkanethiol self-assembled monolayer (SAM) channel with monolayer graphene and a ferroelectric polymer gate. The ferroelectric polarization of the top gate allows for nonvolatile modulation of the Fermi level of the graphene relative to the molecular orbitals. This also enables reversible switching between hole- and electron-dominant conduction pathways within the same molecular channel, effectively creating an ambipolar switch. The switching conduction can be reconfigured on-demand by both gate and drain biases, as well as the molecular species. The device exhibits stable nonvolatile switching endurance over 100 cycles and retention for 10^3 s. Furthermore, leveraging the gate-tunable analog conductance states and nonvolatile characteristics, we present a proof-of-concept demonstration of synaptic plasticity, achieving ∼84.37% accuracy and ∼5.98 μJ of vector-matrix multiplication (VMM) energy per image in a Fashion-MNIST pattern recognition task. This work demonstrates a solid-state vertical molecular device for nonvolatile ambipolar transistors, supporting advanced reconfigurable in-memory computing and neuromorphic electronics utilizing molecular-scale channels.**

KEYWORDS: *molecular electronics, molecular transistor switch, reconfigurable ambipolar transistor, molecular heterojunction, ferroelectric polarization modulation, synaptic plasticity*

INTRODUCTION

The pursuit of controlling charge transport at an ultimate electronic scale has propelled the advancement of the contemporary semiconductor industry since its inception.[1−4] As conventional semiconductor architectures and channels approach their physical scaling limits, molecular electronics has emerged as one of the promising routes for ultimate miniaturization through the bottom-up approach,[5,6] offering molecular-scale channels,[7,8] quantum-level transport phenomena[9,10] and the versatility of chemical design.[11−15] The cornerstone of modern electronic devices begins with constructing a field-effect transistor (FET) where an external gate node modulates the charge density of the channel by shifting its energy bands relative to the Fermi level (E_F) of the electrodes.[16−18] By exploiting a molecular-scale channel,

Received: October 1, 2025
Revised: November 17, 2025
Accepted: November 18, 2025
Published: November 24, 2025

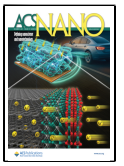

Downloaded via SEOUL NATL UNIV on February 1, 2026 at 02:46:15 (UTC).
See https://pubs.acs.org/sharingguidelines for options on how to legitimately share published articles.

© 2025 American Chemical Society

https://doi.org/10.1021/acsnano.5c16879
ACS Nano 2025, 19, 41386−41395

diverse methodologies for the implementation of the molecular transistor have been proposed and demonstrated more for the past few decades. For example, Park et al. developed a single molecular FET by patterning electromigrated Au nanogap electrodes with a Si back gate, demonstrating gate-tunable Coulomb blockade conduction.[19] Guo et al. have developed a method for covalently interconnecting a conducting molecule with gaps in single-walled carbon nanotubes.[20] This device enables reversible conductance switching via back gate modulation of the interfacial Schottky barrier. Song et al. demonstrated the direct manipulation of molecular orbitals via back-gate modulation in a single-molecule transistor, which allows for changes in the effective barrier height based on the magnitude of the gate voltage.[12] These all-suggested methods can provide testbeds for investigating the field-effect electrical characterization of various molecular species. In addition, these demonstrations have facilitated scientific breakthroughs and significant engineering progress in functional molecular-scale transistors and their applications. Nonetheless, significant hurdles persist, including the manufacturability of large-scale devices, stable contact formation, efficient gating modulation, and operation at room temperature, which must be addressed to realize commercially viable molecular transistors.[21] Moreover, these molecular transistors frequently encounter low device yields and considerable fluctuations in conductance due to the necessity of lateral bridging molecules in the nanogaps, which can severely restrict their applicability.[22,23]

Recently, vertical configurations of molecular self-assembled monolayers (SAMs)-based transistors have been proposed to address these challenges in lateral molecular transistors. This method does not require a predefined lateral nanogap configuration; instead, it intrinsically establishes the gap through the thickness of the molecular layer itself. It may enable a high-efficiency and reliable platform for molecular transistors. For example, Jia et al. demonstrated a vertical molecular transistor gated by an ionic liquid, achieving reliable and room-temperature tunneling switching with stable contact formation.[24] Similarly, Kim et al. developed a vertical molecular transistor that integrates mixed alkanethiol-based SAMs in ion-gel-gated Au/graphene stacks.[25] In this transistor, the net dipole of the mixed SAMs improved gating efficiency by suppressing the field screening effect, clearly observing a transition from direct to Fowler−Nordheim tunneling regime using ion gel gating. However, reliance on an ionic liquid gate may present challenges concerning high-density devices and the fabrication of large-scale arrays, which are essential for contemporary electronic applications.[22−26] Therefore, the development of solid-state vertical molecular transistors is essential for progressing to the next stage of molecular electronics.[22]

In general, the majority of carriers in the previously developed molecular transistors are challenging to change because of the constrained gating modulation range and the dominant molecular orbital path initially formed in their junction geometries.[22] These inherent limitations may impede the expandability and applicability of the molecular transistors, especially for the construction of complementary molecular FETs. For example, integrating n- and p-type molecular transistors within a single device framework using two distinct molecular components may pose challenges in its fabrication complexity and the programming coherence between two types.[26] Given these unavoidable issues, the development of a novel molecular ambipolar transistor offers a compelling alternative because it possesses the unique characteristic of allowing both types of carriers to be transported simultaneously and selectively within the channel.[27] Therefore, it can integrate the functionalities of both n- and p-type transistors within a singular device regardless of the operational coherence between them, thereby potentially streamlining device fabrication and lowering production costs in comparison to complementary molecular FET technology that requires precise matching and integration of separate p-type and n-type devices.[28,29] Furthermore, if the nonvolatile switching capability is integrated into the molecular ambipolar transistor, its range of applications could significantly expand. For example, these functionalities may facilitate their utilization in reconfigurable in-memory computing and neuromorphic electronics. Despite such potential, there are rarely reports regarding nonvolatile molecular ambipolar transistors. Rather, due to the structural and functional challenges of the three-terminal molecular transistor switch, two-terminal molecular junctions based on redox-active molecules have been recently employed to demonstrate reconfigurable and neuromorphic functionalities.[30−32] These behaviors originate from proton-coupled electron transfer processes, exhibiting hysteretic conductance modulation and synaptic-like plasticity.[30−32] However, such functionality strongly depends on the intrinsic properties of specific molecular systems, and achieving stable operation typically requires soft liquid-metal electrodes such as eutectic gallium−indium (EGaIn), which presents challenges for scalable and solid-state integration. In this context, it is important to design and develop a novel solid-state vertical molecular ambipolar transistor that possesses reconfigurable nonvolatile characteristics. Building upon these molecular junction approaches, vertical molecular transistor architectures have a potential to enhance tunability and design freedom by enabling external electrostatic control of molecular channels through a gate electrode.

In this study, we report on the design and fabrication of a three-terminal solid-state vertical molecular ambipolar transistor switch. This device architecture integrates an alkanethiol SAMs channel of 1−2 nm with a monolayer graphene electrode and a ferroelectric polymer top gate. The remnant polarization of the ferroelectric polymer, which can be gradually adjusted by the electrostatic gating, is used to nonvolatilely shift the E_F of the graphene compared to the molecular orbitals of the SAMs. This enables reversible switching between hole- and electron-dominant conduction pathways within a single device framework, demonstrating the gate-controlled ambipolar switching. This gate-controlled switching can be also reconfigured on demand through the drain voltage and molecular species. Leveraging these characteristics, we successfully implement long-term potentiation and depression (LTP/LTD) behaviors, and as a proof-of-concept, simulate a neural network for pattern recognition. This study introduces an innovative solid-state vertical molecular device for nonvolatile ambipolar transistors, facilitating progress in sophisticated reconfigurable in-memory computing and neuromorphic electronics that employ molecular-scale channels.

RESULTS/DISCUSSION

Here, we designed and fabricated a novel structure of reconfigurable molecular ambipolar transistor switches (240 cells on a single device chip) comprising a vertical stacked mixed-dimensional structure of Al/P(VDF-TrFE)/monolayer

https://doi.org/10.1021/acsnano.5c16879
ACS Nano 2025, 19, 41386−41395

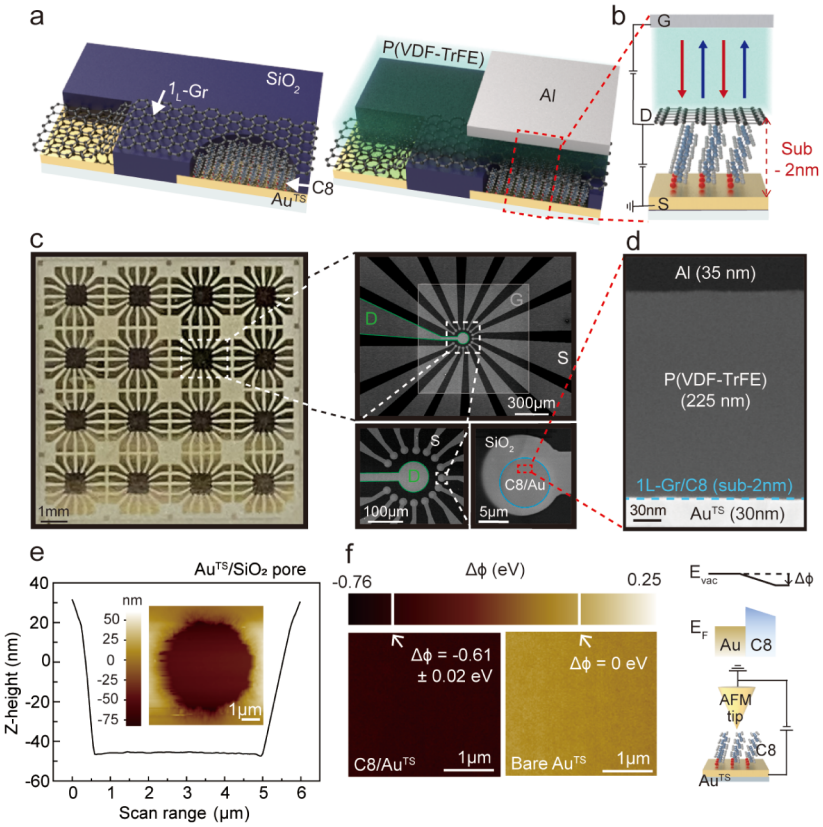

Figure 1. Schematics of the fabricated molecular ambipolar transistor switch. (a) Schematic illustrating the bottom-up approach for the mixed-dimensional vertical molecular transistor: (left) formation of 1_L-Gr/C8 SAMs/Au^{TS} stack and (right) subsequent deposition of the P(VDF-TrFE) ferroelectric polymer and Al top gate. (b) Cross-sectional schematic of the vertical molecular transistor switch. (c) Optical image of 240 molecular transistor switches on a 1 × 1 cm^2 chip (left) and SEM images of the 16-unit devices pattern (top right), the radial arrangement of 15 sources (S) around one shared drain (D) and gate (G) (bottom left), and a magnified view of a single via-hole defining the molecular junction (bottom right). (d) Cross-sectional TEM image of a single vertical molecular transistor, displaying well-defined layers in the structure (Al (35 nm), P(VDF-TrFE) (225 nm), 1_L-Gr/C8 (sub-2 nm), and Au^{TS} (30 nm)). (e) Topographical line profiles across a via-hole into the SiO_2 layer on an Au^{TS} electrode obtained from noncontact AFM. Inset shows the corresponding 2D AFM image. (f) Surface potential images of bare Au^{TS} and C8/Au^{TS} obtained by scanning Kelvin probe microscopy (SKPM) (left), demonstrating a work function shift due to the SAM formation. Schematics (bottom right) illustrates the SKPM setup and corresponding energy band diagram indicating the change in work function (top right).

graphene (1_L-Gr)/molecules/Au^{TS}. The device incorporates a one-dimensional (1D) molecular SAMs channel, a two-dimensional (2D) monolayer graphene (1_L-Gr) electrode, and a three-dimensional (3D) ferroelectric polymer used as the gate dielectric. As shown in Figure 1a,b, these mixed-dimensional layers are vertically stacked to form a three-terminal transistor switch structure, which is advantageous for achieving scalable integration and high device density. This 1D/2D/3D vertically stacked heterostructure possesses compatibility with sequential large-scale fabrication for developing a vertical molecular transistor in solid-state device systems.

In this device architecture, the alkanethiol molecular SAMs (e.g., octanethiol (C8)) serve as a vertical channel (sub-2 nm) that is formed by chemisorption onto a patterned template-stripped Au (Au^{TS}) electrode (source). The utilization of Au^{TS} substrate enhances the quality of the molecular assembly by providing an ultraflat surface,[33−35] as demonstrated by atomic force microscopy (AFM) analysis (see Figures S1 and S2). The 1_L-Gr was transferred onto the molecular SAMs and serves as a drain electrode as well as barrier modulator (the left scheme of Figure 1a). In addition, it can be also utilized as a separation layer for preventing unwanted interfacial formation and sustaining interfacial integrity. Subsequently, a spin-coated P(VDF-TrFE) layer was deposited onto the 1_L-Gr and served as a gate ferroelectric layer (the right of Figure 1a). The direction of the ferroelectric domains in this layer can be changed by an electric field, endowing it with reconfigurable switching states (Figure 1b).[36−38] The P(VDF-TrFE) copolymer used here exhibits the electro-active β-phase, yielding a remnant polarization and moderate coercive field at room temperature (Figure S3).[39−41] These strong ferroelectric properties enable the film to retain nonvolatile dipole orientation, which is expected to alter the position of the E_F of 1_L-Gr with respect to the molecular orbitals. Then, a patterned top Al metal was deposited onto the P(VDF-TrFE) layer using a shadow mask and played as a top gate electrode (the right of Figure 1a,b). This vertical mixed-dimensional heterostructure can provide a solid-state molecular vertical transistor configuration that can extend into large-scale fabrication while minimizing damage to the molecular SAMs itself.

Figure 1c shows an optical image (left) of the fabricated 240 reconfigurable molecular ambipolar transistor switches on a 1 × 1 cm^2 substrate. A total of 16 units is patterned on the substrate, each consisting of one shared global drain (D) and gate (G) electrode, connected to 15 individual source (S)

https://doi.org/10.1021/acsnano.5c16879
ACS Nano 2025, 19, 41386−41395

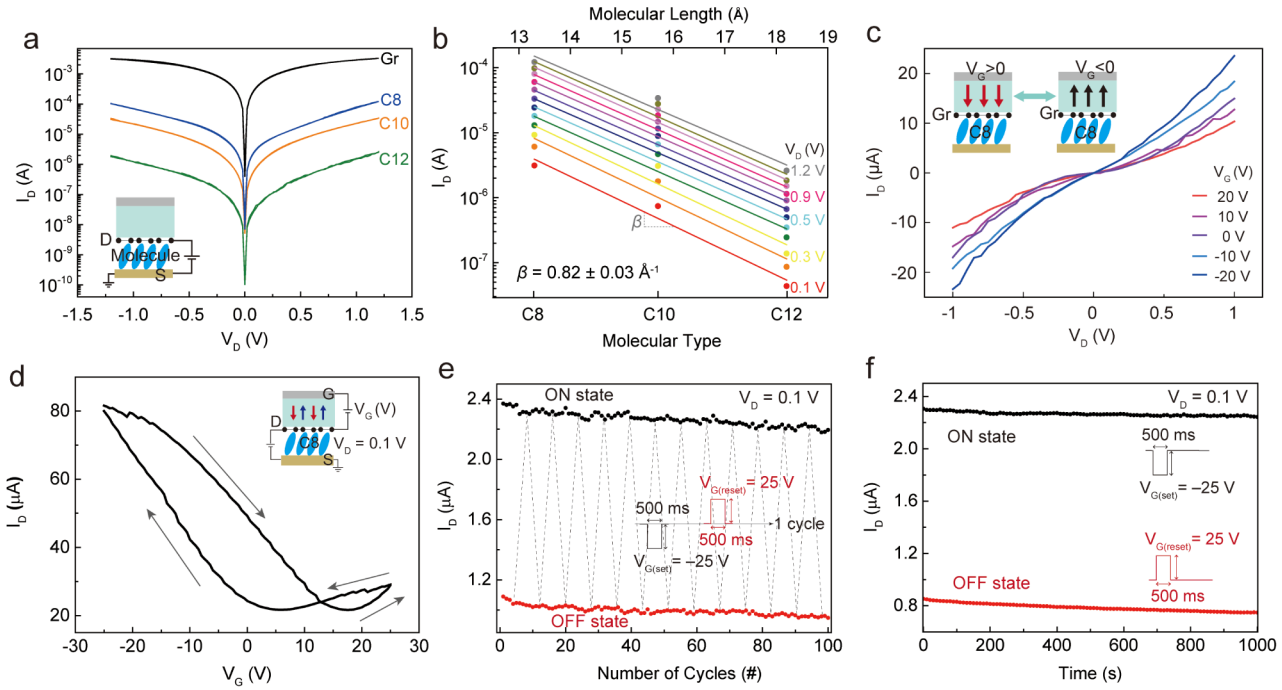

Figure 2. Switching characteristics of the molecular transistor switch. (a) Representative I_D−V_D of the molecular transistor switch with different molecular lengths (C8 (blue), C10 (orange), and C12 (green)), highlighting length-dependent tunneling transport through the molecular SAMs. A direct Gr/Au junction without molecules is expressed in black line. Inset shows the schematic of the device measurement setup. (b) Semilog plot of I_D as a function of molecular length for C8, C10, and C10 SAMs at different V_D. The extracted tunneling decay coefficient (β) is 0.82 ± 0.03 Å^{-1}. (c) Representative I_D−V_D of the C8 transistor switch under various V_G from −20 to 20 V, demonstrating gate-tunable transport behavior. Inset shows ferroelectric dipole orientations in the P(VDF-TrFE) under positive (left) and negative (right) V_G. (d) Representative I_D−V_G switching curve of the C8 transistor switch at V_D = 0.1 V with V_G swept between ±25 V, originated from voltage-history-dependent ferroelectric polarization. (e) Endurance of ON and OFF states for the C8 transistor switch over 100 cycles. (f) Retention of ON and OFF states for 10^3 s. The programming gate voltages are set to $V_{G(set)}$ = −25 V for 500 ms and $V_{G(reset)}$ = 25 V for 500 ms, and the read condition is V_D = 0.1 V at V_G = 0 V.

electrodes arranged radially, as shown in the scanning electron microscope (SEM) images of Figure 1c. The global drain is connected to the 1_L-Gr layer, and the gate voltage (V_G) modulates the ferroelectric polarization of the P(VDF-TrFE) layer underneath the top Al electrode. A cross-sectional transmission electron microscopy (TEM) image of a selected junction reveals the stacked structure of Al (~35 nm)/P(VDF-TrFE) (~225 nm)/1_L-Gr/C8/Au^{TS} (Figure 1d). The C8 SAMs are localized within isolated micro via hole (~5 μm) structures etched into the SiO_2 (~100 nm) layer (Figure 1c,e, and Figure S1). The C8 thickness is known to be ~1.2 nm[42−44] which is marked with a dashed blue line of Figure 1d. To verify the successful formation of the C8 SAMs on the Au^{TS} electrode, scanning Kelvin probe microscopy (SKPM) measurement was performed on both bare Au^{TS} and C8 SAMs/Au^{TS} substrate (Figure 1f). The surface potential ($\Delta\phi$) of the C8 SAMs/Au^{TS} decreases by −0.61 eV relative to bare Au, and its direction and magnitude agree well with previous results.[45,46]

The electrical characteristics of the vertical molecular transistor switches is investigated with different molecular SAMs species and various programming schemes. Figure 2a shows the output characteristics (I_D−V_D) of the vertical molecular transistor switches incorporating different alkanethiol molecular species (1-octanethiol (C8), 1-decanethiol (C10), and 1-dodecanethiol (C12)) in comparison with a junction lacking the molecular layer (1_L-Gr/Au). The presence of the molecular SAMs introduces a tunneling barrier, exhibiting a nonlinear length-dependent transport behavior with lower current levels than that of 1_L-Gr/Au junction. Therefore, the molecular channel could significantly influence the conductance of the molecular transistor switches, allowing a high degree of its reconfigurability. The tunneling decay coefficient for this molecular transistor switch that reflects how much the change wave function exponentially decreases with the molecular length is found to be 0.82 ± 0.03 Å^{-1} (Figure 2b), which is comparable to previously reported values for only alkanethiol-based molecular junctions.[47,48] This coefficient is comparable to the fitting value extracted from the linear fit of ln(J) versus molecular-backbone length (L), where the contact current density (Jo) is found to be 1.12 ± 0.74 × 10^9 Am^{-2} (Figure S4). This indicates that the molecular transistor switch exhibits the intrinsic tunneling conduction behavior through the molecular barrier itself, confirming its suitability as a molecular device platform. The conductance of the molecular transistor switch can be also controlled by a gate, using a ferroelectric P(VDF-TrFE) layer as the top gate insulator. Figure 2c shows the I_D−V_D characteristics of the molecular transistor switch consisting of Al/P(VDF-TrFE)/1_L-Gr/C8/Au^{TS} structure upon varied V_G from −20 to +20 V (see also Figure S5 for V_G ranging from −25 to +25 V). Upon application of V_G, the dipole alignment within the P(VDF-TrFE) layer responds to the external electric field, gradually establishing a net polarization direction (Figure S3). The direction of the dipole moment is downward (red arrows) when the V_G is positive, and upward (black arrows) when the V_G is negative, as shown in the inset of Figure 2c. This can differently shift the E_F of the 1_L-Gr with respect to the

https://doi.org/10.1021/acsnano.5c16879
ACS Nano 2025, 19, 41386−41395

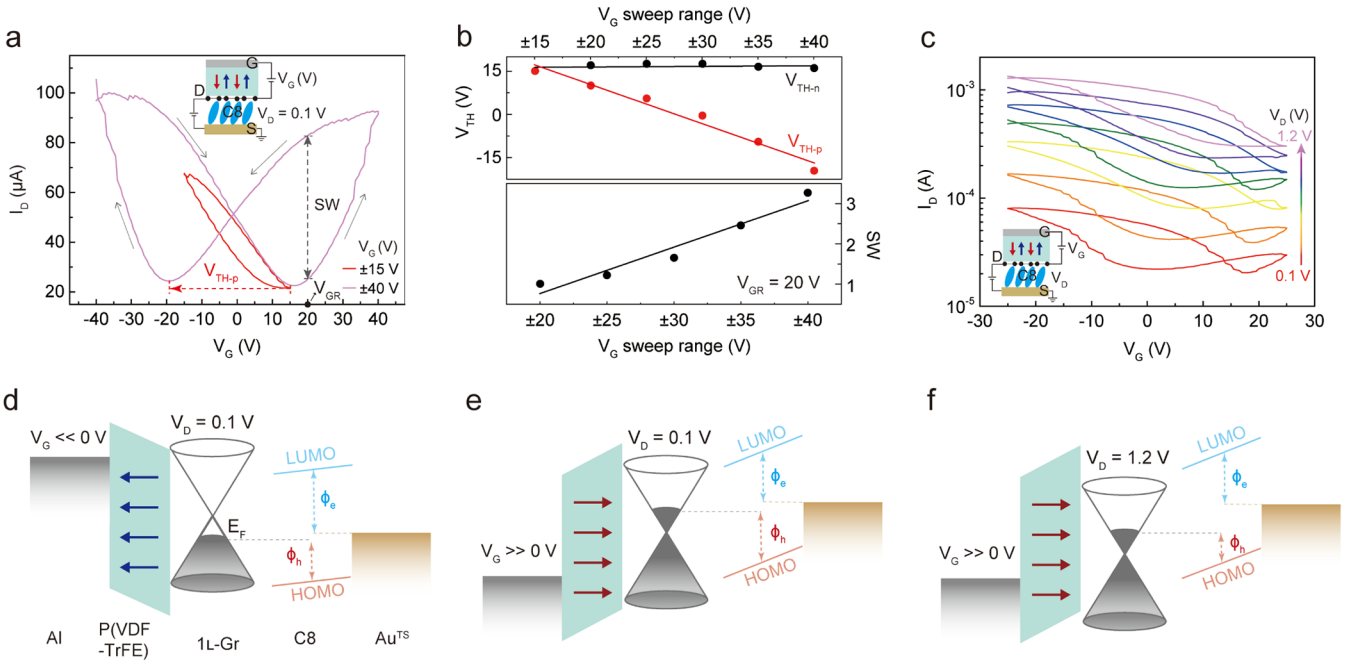

Figure 3. Reconfigurable ambipolar transport characteristic of the molecular transistor switch. (a) I_D−V_G switching curve of the C8 transistor switch at V_D = 0.1 V with different V_G sweep ranges of ±15 V (red, exhibiting p-type behavior) and ±40 V (purple, exhibiting ambipolar behavior). The red arrow indicates the threshold voltage at p-type region (V_{TH-p}) and the black arrow indicates the switching window (SW) at V_{GR} = 20 V. Inset shows the schematic of the biasing configuration. (b) (top) Threshold voltages at p-type (V_{TH-p}, red) and n-type (V_{TH-n}, black) switching region, and (bottom) the SW at V_{GR} = 20 V as a function of the V_G sweep range from ±15 V to ±40 V. (c) I_D−V_G switching curve of the C8 transistor switch at a fixed V_G sweep range of ±25 V with varying V_D from 0.1 to 1.2 V. (d−f) Schematic energy band diagrams illustrating the proposed switching mechanism under different bias conditions. (d) $V_G \ll 0$ V and V_D = 0.1 V. (e) $V_G \gg 0$ V and V_D = 0.1 V. (f) $V_G \gg 0$ V and V_D = 1.2 V.

molecular orbital levels. Given that charge transport through the alkanethiol molecular junction is primarily highest occupied molecular orbital (HOMO)-mediated conduction,[14,45,49,50] the modulation of E_F closer to the HOMO level reduces the tunneling barrier and enhances I_D. As V_G decreases from +20 to −20 V, the polarization-induced shift in E_F moves further below the Dirac point, approaching the HOMO level of the molecular channel and resulting in a progressive increase in I_D. Note that the details of the polarization-dependent charge transport mechanism through this device are further explained in the following section. Figure 2d shows the representative I_D−V_G transfer characteristics of the C8 molecular transistor switch at V_D = 0.1 V, exhibiting a switching hysteresis loop (arrows) through the HOMO-mediated pathway, exhibiting a higher I_D at V_G = −25 V than that at V_G = +25 V (p-type switching). This hysteresis originates from the voltage-history-dependent polarization alignment of the ferroelectric layer, which in turn modulates the E_F of the 1_L-Gr across successive sweeps.[38,51] In this result, different tunneling barrier heights can be formed by the gate-tunable position of E_F with respect to the HOMO level of C8 SAMs. For example, negative (positive) V_G causes the E_F of the 1_L-Gr to shift downward (upward), thereby decreasing (increasing) the barrier height and increasing (decreasing) I_D (Figure S6). Since the dipole alignment of the P(VDF-TrFE) layer is well sustained even after V_G is turned off, it is expected that the molecular transistor switch exhibits nonvolatile nature with distinct ON and OFF current levels. Figure 2e shows the endurance test of the switching states (ON and OFF) for C8 molecular transistor switch over 100 cycles of the programming pulses. Each switching state is read out at V_G = 0, and the programming set ($V_{G(set)}$) and reset ($V_{G(reset)}$) pulses are set to ±25 V for 500 ms, as shown in the inset of Figure 2e. These switching states are well maintained for 10^3 s (Figure 2f), exhibiting robust polarization stability and nonvolatile control of the C8 molecular transistor switch.

Notably, this HOMO-mediated (p-type) C8 molecular transistor switch can function in ambipolar transport under specific V_G conditions. Figure 3a shows the I_D−V_G transfer characteristics of the C8 molecular transistor switch at V_D = 0.1 V with two V_G sweep ranges of ±15 V and ±40 V. When the V_G is double swept from −15 V to +15 V, the C8 molecular transistor switch exhibits dominant HOMO-mediated (p-type) ferroelectric switching behavior. This signifies that the position of the graphene's E_F even within the applied V_G range (from −15 to +15 V) remains in proximity to the HOMO level of C8 SAMs, maintaining the p-type conduction (Figure S6). Interestingly, however, when the applied V_G range changes to ±40 V, the predominant p-type switching behavior transitions to ambipolar switching and the threshold voltage (V_{TH-p}) in the p-type region shifts from 15 to −19.5 V (the red arrow of Figure 3a). As shown in the top of Figure 3b, the V_{TH-p} at the p-type switching region (red circles) is gradually decreased upon the change of V_G condition from ±15 to ±40 V (see Figure 3 and Figure S7). However, the V_{TH-n} at the n-type switching region (black circle) remains unchanged near ∼15 V regardless of the magnitude of the V_G range while the switching window (SW) at V_{GR} = 20 V (the gate-read voltage) is increased as the V_G increases, as shown in the bottom of Figure 3b. Statistical analysis on V_{TH-p}, V_{TH-n}, and SW for the several C8 molecular transistor switches are described in Figure S8. Therefore, in this molecular transistor switch, it can

https://doi.org/10.1021/acsnano.5c16879
ACS Nano 2025, 19, 41386−41395

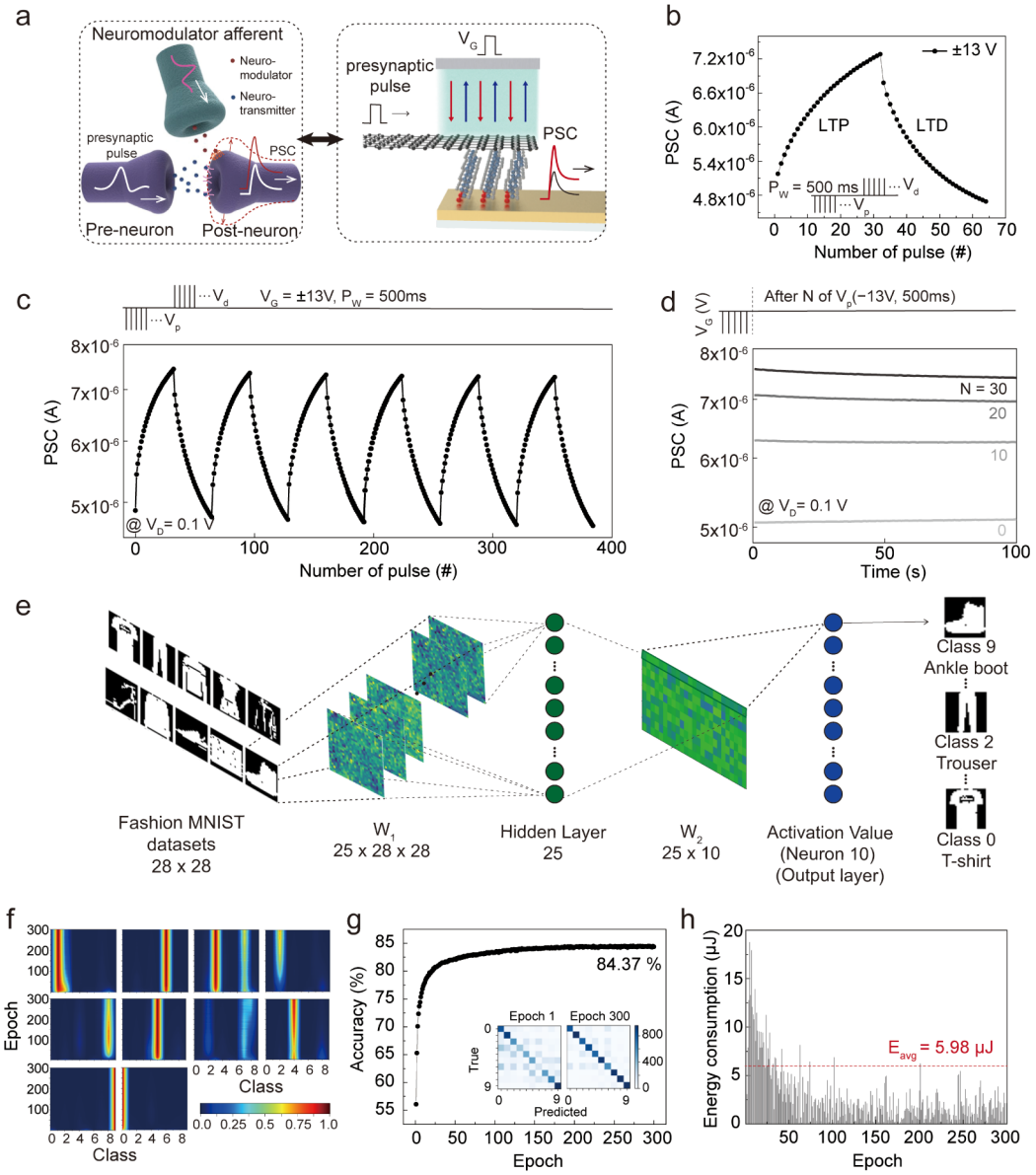

Figure 4. Neuromorphic application based on the molecular ambipolar transistor switch. (a) Schematics of a biological synapse with neuromodulator afferent (left) and the fabricated molecular transistor switch (right). (b) A single transition of LTP and LTD function of PSC at V_D = 0.1 V for the C8 molecular transistor switch in response to 32 potentiating (V_p = −13 V) and 32 depressing (V_d = 13 V) pulses with P_W = 500 ms. (c) Repeated six cycles of LTP and LTD function of PSC at V_D = 0.1 V using same V_G pulses scheme as in (b). (d) Retention of multiple PSC states at V_D = 0.1 V after N (0, 10, 20, and 30) potentiating pulses (V_p = −13 V for 500 ms), showing nonvolatile behavior over 100 s. (e) Schematic of the ANN architecture used for Fashion-MNIST image recognition, consisting of 784 input neurons, 25 hidden neurons, and 10 output neurons. The synaptic weight maps (W_1 and W_2) are updated based on experimental measured PSC values. (f) Output distribution of the 10 fashion classes as a function of training epochs. Color scale indicates activation level. (g) Recognition accuracy for the Fashion-MNIST images as a function of training epochs. Inset shows the confusion matrices between predicted and true labels at epoch 1 and epoch 300. (h) Energy consumption per image for the VMM operation during inference as a function of training epochs.

effectively attain ambipolar switching behavior via electrostatic modulation of the E_F of the 1_L-Gr in relation to the molecular orbitals in a nonvolatile manner, even with a conventional molecular SAMs structure (i.e., alkanethiols). Note that C10 molecular transistor switch (Figure S9), with a longer alkanethiol SAM channel, yields about one order lower current with exhibiting a similar gate-tunable ambipolar switching and nonvolatile behavior as the C8 devices. The switching behavior of the C8 molecular transistor switch can also be reconfigured by the application of V_D itself. Applying the V_D across the junction can directly create a potential difference between top (D) and bottom (S) electrodes, modifying the effective tunneling barrier. Figure 3c shows the I_D−V_G transfer characteristics of the C8 molecular transistor switch as the V_D increases from 0.1 to 1.2 V under the fixed V_G range of ±25 V. An elevated V_D increases I_D at the same V_G and progressively enhances the predominant conduction characteristic toward p-type behavior. Namely, the n-type switching behavior gradually diminishes as the V_D increases from 0.1 to 1.2 V.

https://doi.org/10.1021/acsnano.5c16879
ACS Nano 2025, 19, 41386−41395

The underlying transport mechanism for the ambipolar transport behavior can be understood from the band diagrams at different V_G, as shown in the schematics of Figure 3d,e. When the $V_G \ll 0$ V, the dipole direction of the P(VDF-TrFE) layer aligns to the left (indicated by the blue arrows), which shifts the E_F of 1_L-Gr below the Dirac point and closer to the HOMO level of C8 SAMs (Figure 3d). This can further reduce the hole barrier (ϕ_h or E_F-HOMO level), facilitating hole dominant tunneling. When the $V_G \gg 0$ V, the dipole direction of the P(VDF-TrFE) layer aligns to the right (indicated by the red arrows), which shifts the E_F of 1_L-Gr above the Dirac point and closer to the LUMO level of C8 SAMs (Figure 3e). This gate modulation has the potential to reduce the electron barrier (ϕ_e or LUMO-E_F), greatly increasing the degree of electron tunneling in the total conduction, which causes the ambipolar transport behavior. Since the initial E_F position of 1_L-Gr closely situated near the HOMO level of C8 SAMs, a positive V_G is necessary to shift the E_F to its HOMO−LUMO midgap. This explains why the C8 molecular transistor switch can exhibit a positive $V_{TH\text{-}p}$ under initial conditions. However, when a larger positive V_G is applied, the amount of ferroelectric domains in the P(VDF-TrFE) layer that point downward further increases. This indicates that a stronger opposing field (i.e., negative V_G) may be needed to depolarize the ferroelectric layer and bring the E_F back to the HOMO−LUMO midgap. This elucidates the transition of $V_{TH\text{-}p}$ from positive to negative V_G within the p-type switching region (as depicted at the top (red circles) of Figure 3b). However, even with the application of a more negative V_G to shift the E_F closer to the HOMO level of C8 SAMs, the $V_{TH\text{-}n}$ in the n-type switching region remains largely unaffected (as depicted at the top (black circles) of Figure 3b). We suspect that this phenomenon occurs because the E_F position of the 1_L-Gr approaches saturation near the HOMO level of C8 SAMs, which may be caused by the complete upward shift of the ferroelectric domains under these programming regimes. With the same basis, the application of higher V_D can shift the E_F of the 1_L-Gr close to the HOMO level of C8 SAMs even at higher positive V_G ($V_G \gg 0$ V), as shown in Figure 3f. This can further strengthen the p-type switching behavior and account for the absence of ambipolar characteristics noted at higher V_D (Figure 3c). In fact, the capacity to reversibly modulate carrier types and memory states through both V_G and V_D control could simplify on-demand device design while simultaneously expanding electronic functionality.

Since the conductance of the molecular transistor switch can be gradually reconfigured with different V_G and V_D conditions and has a nonvolatile nature owing to the aligned ferroelectric domains by the applied electric field, it has the potential to be utilized in a brain-inspired computing application (Supporting Note S1). As a proof-of-concept, the solid-state vertical molecular transistor was leveraged for its nonvolatile and gate tunable conduction via V_G pulse sequences to emulate analog synaptic behavior. Figure 4a illustrates the conceptual and functional analogy between a biological synapse connected with a neuromodulator afferent (left) and the molecular transistor switch (right) consisting of a vertical stacked mixed-dimensional structure of Al/P(VDF-TrFE)/1_L-Gr/C8 SAMs/Au^{TS}. In the biological synapse, the synaptic weight is regulated through chemical signals such as neurotransmitters and neuromodulators between pre- (or afferent) and postneurons in response to stimuli.[52] Inspired by this underlying principle in controlling the synaptic weight between neurons, the C8 SAMs and the P(VDF-TrFE) of the molecular transistor switch play roles as the synaptic channel and the neuromodulator, respectively. The change in the magnitude of neuromodulator released from the afferent in the biological synapse can be mimicked by the change in the polarization of the ferroelectric domain of the P(VDF-TrFE) layer, which can be controlled by the V_G input conditions.[36,53,54] According to the applied V_G, the interfacial tunneling barrier at 1_L-Gr/C8 SAMs is adjusted, changing the magnitude of the postsynaptic current (PSC) at a fixed V_D that reflects the strength of the synaptic weight. Therefore, in our designed transistor switch, it is possible to reconfigure the synaptic weights depending on the V_G pulse conditions in an analog manner. Figure 4b shows an example of a single transition between long-term potentiation (LTP) and depression (LTD) of the PSC at V_D = 0.1 V for the C8 molecular transistor switch. The V_G pulse trains were composed of 32 potentiating (V_p = −13 V) and 32 depressing (V_d = 13 V) pulses, each with a pulse width (P_w) of 500 ms, making individual 32 PSC states. When the negative V_p gate pulses are continuously applied, the dipole moment of the ferroelectric domains gradually aligns to the upward direction, bringing the E_F of 1_L-Gr even closer to the HOMO level of C8 SAMs. As a result, the magnitude of the PSC increases. However, when the positive V_d gate pulses are continuously applied, all the dipoles are reversely changed, leading to the decrease of the PSC. Using the repeated $V_{p(d)}$ pulse scheme, the stable and repeated transition between LTP and LTD function during 384 pulses (6 cycles) is demonstrated, as shown in Figure 4c. In addition, the updated PSC values according to the different programming numbers of V_p pulses (N = 0, 10, 20, and 30) are well maintained for 100 s without significant degradation in the states (Figure 4d). It demonstrates the nonvolatile and cumulative properties of ferroelectric polarization via gate modulation of the device.

To evaluate the learning capability of the molecular transistor switch, we performed the pattern recognition task for 10 Fashion-MNIST image data sets using a standard supervised backpropagation (BP) learning algorithm.[55−58] The artificial neural network (ANN) for the image recognition process was configured with 784 input neurons (corresponding to 28 × 28 pixels), 25 hidden neurons, and 10 output neurons, as shown in Figure 4e. The first weight map (W_1) connecting the input-to-hidden layers consists of the dimension of 25 × 28 × 28, while the second weight map (W_2) connecting the hidden-to-output layers consists of the dimension of 25 × 10. Note that the updated W_1 and W_2 values are obtained from experimentally measured PSC characteristics in the LTP and LTD function for the C8 molecular ambipolar transistor switch. The trained W_1 as a function of epochs from 1 to 300 is shown in the Supporting Information (Figure S10), which can project the input image matrix (28 × 28) into 25 hidden neurons. The activation values from the 25 hidden neurons serve as intermediate features and are subsequently transmitted through the W_2 (25 × 10) to generate 10 outputs corresponding to 10 MNIST Fashion images (Figure S11). The distribution of W_2 was updated appropriately and stably with increasing epochs, reflecting progressive adaptation to the classified image data sets (Figures S12−S14). Figure 4f shows the output distribution of the 10 fashion classes as a function of the training epoch, demonstrating class-wise neuron selectivity and well-defined class discrimination. Note that the color scale reflects the activation level of each output neuron, where red (1.0) indicates higher activity and blue (0.0) indicates lower

https://doi.org/10.1021/acsnano.5c16879
ACS Nano 2025, 19, 41386−41395

activity. Using these trained W_1 and W_2 maps, the molecular transistor switch-based ANN can reach about 84.37% accuracy after 300 epochs for the recognition of the 10 Fashion-MNIST image data sets, which is comparable to results found in earlier studies. This result can be further confirmed in the confusion matrix between predicted and true labels obtained at epochs of 1 and 300, respectively, as shown in the insets of Figure 4g. Note that the inference loss curve and the additional confusion matrix according to the number of epochs are described in Supporting Information (Figures S15−S17).

We also investigated the total accumulated energy consumption of the vector-matrix multiplication (VMM) operation[36,59] for the C8 molecular transistor switch-based ANN for inferring the 10 Fashion-MNIST image data sets. As shown in Figure 4h, the VMM energy overall decreases as the number of epochs increases, indicating the weight maps are almost updated. The average VMM energy per image was approximated 5.98 μJ for the 300 epochs. In fact, the energy consumption of VMM is significantly influenced by the magnitude of the conductance states; thus, we assert that it can be effectively and substantially modified by regulating the molecular length (Figure 2a and Figure S9) and the programming scheme (Figure 3c). Note that the thickness of the P(VDF-TrFE) layer can be further reduced to sub-10 nm when the substrate provides smoothness and high surface energy that promote uniform wetting and stable nucleation. This reduction is expected to lower the operating voltage in our molecular transistor switch as well as the VMM energy. Such a flexible controlling ability in the suggested molecular transistor switch could help to improve energy efficiency for low-power brain-inspired computing systems. In summary, these results indicate that the reconfigurable molecular ambipolar transistor switch can facilitate the synaptic weight update process due to its analog nonvolatile characteristics as well as offer a promising pathway for the ultimate scaling benefits of molecular-scale channels.

CONCLUSIONS

In this work, we have successfully engineered and demonstrated a novel solid-state vertical molecular transistor architecture that achieves reconfigurable nonvolatile ambipolar switching, a significant step forward in molecular electronics. By precisely integrating an alkanethiol SAMs channel with the 1_L-Gr electrode and a P(VDF-TrFE) ferroelectric top gate, we have gained unprecedented control over the dominant charge carrier type—hole or electron—within a single molecular device framework. The key to this functionality lies in the nonvolatile, history-dependent modulation of the E_F of the 1_L-Gr by the ferroelectric gate's remnant polarization, which strategically positions it relative to the molecular orbitals. This fine-tuned electrostatic control not only enables reversible switching between p-type and n-type dominant conduction but also creates distinct and stable analog switching states. The molecular ambipolar transistor switch demonstrates good endurance in switching states for over 100 cycles and maintains these states for 10^3 s, highlighting its suitability for practical molecular memory applications. Beyond this, we have also utilized these unique electrical phenomena in a compelling demonstration of neuromorphic functionality. Especially, the analog conductance modulation and nonvolatile characteristics were harnessed to emulate synaptic functions such as LTP and LTD. This synaptic mimicry was further validated through a proof-of-concept neural network simulation for Fashion-MNIST image recognition, which achieved a notable accuracy of ∼84.37% and an average VMM energy of ∼5.98 μJ per image. These results vividly illustrate the potential of our molecular ambipolar transistor switch as building blocks for energy-efficient, in-memory computing architectures and sophisticated brain-inspired electronic systems utilizing molecular-scale channel.

METHODS/EXPERIMENTAL

Sample Preparation. Self-assembled monolayers (SAMs) of three molecular alkanethiols C8, C10, and C12 were obtained from Sigma-Aldrich Korea. The alkanethiol molecules formed densely packed monolayers on a micro pore Au bottom electrode. The SAMs were formed on the template stripped Au (Au^{TS}) bottom substrate. The monolayers exhibited a grafting density N_0 of 4.65×10^{18} m^2 for the C8 monolayer. 1_L-Gr used as the top contact was synthesized by chemical vapor deposition (CVD) and transferred onto the target substrates by a standard wet transfer procedure. The ferroelectric polymer layer was prepared using poly vinylidene fluoride trifluoroethylene P(VDF-TrFE) (75:25 wt %, Sigma-Aldrich Korea). The polymer was dissolved in *N,N*-dimethylformamide (DMF, Sigma-Aldrich Korea) to prepare the ferroelectric polymer solution. The ferroelectric gate layer was prepared by casting the solution and spin coating, followed by thermal annealing at 120 °C to induce ferroelectric crystalline ordering. Detailed fabrication process, device characterization, and simulation method are described in Supporting Information.

ASSOCIATED CONTENT

Data Availability Statement

All data needed to evaluate the conclusions in the paper are present in the paper and/or the Supporting Information.

Supporting Information

The Supporting Information is available free of charge at https://pubs.acs.org/doi/10.1021/acsnano.5c16879.

Additional experimental details; characterization data; electrical results; neural network analysis; supplemental figures and references (PDF)

AUTHOR INFORMATION

Corresponding Author

Gunuk Wang − *KU-KIST Graduate School of Converging Science and Technology, Korea University, Seoul 02841, Korea; Department of Integrative Energy Engineering, Korea University, Seoul 02841, Korea;* orcid.org/0000-0001-6059-0530; Email: gunukwang@korea.ac.kr

Authors

Jung Sun Eo − *KU-KIST Graduate School of Converging Science and Technology, Korea University, Seoul 02841, Korea; Department of Materials Science and Metallurgy, University of Cambridge, Cambridge CB3 0FS, United Kingdom*

Takgyeong Jeon − *KU-KIST Graduate School of Converging Science and Technology, Korea University, Seoul 02841, Korea*

Young Ran Park − *KU-KIST Graduate School of Converging Science and Technology, Korea University, Seoul 02841, Korea;* orcid.org/0000-0002-5816-1988

Hyeon Bin Kim − *KU-KIST Graduate School of Converging Science and Technology, Korea University, Seoul 02841, Korea*

https://doi.org/10.1021/acsnano.5c16879
ACS Nano 2025, 19, 41386−41395

Eunyoung Lee − *Functional Composite Materials Research Center, Korea Institute of Science and Technology (KIST), Wanju-gun, Jeollabuk-do 55324, Republic of Korea*
Sukang Bae − *Functional Composite Materials Research Center, Korea Institute of Science and Technology (KIST), Wanju-gun, Jeollabuk-do 55324, Republic of Korea;* orcid.org/0000-0002-3019-0584
Hyunhak Jeong − *Department of Semiconductor Engineering, Tech University of Korea, Siheung-si, Gyeonggi-do 15073, Republic of Korea*
Takhee Lee − *Department of Physics and Astronomy, and Institute of Applied Physics, Seoul National University, Seoul 08826, Korea;* orcid.org/0000-0001-5988-5219

Complete contact information is available at: https://pubs.acs.org/10.1021/acsnano.5c16879

Author Contributions

[▽]J.S.E. and T.J. contributed equally to this work J.S.E., T.J., and G.W. conceived the project and designed the experiments. J.S.E. and T.J. performed material characterization and investigated the transport properties of the fabricated devices. J.S.E. and G.W. led the writing of the manuscript. Y.R.P. conducted the pattern recognition simulations with assistance in schematic illustration. H.B.K. contributed to the graphene material preparation in the experiments and assisted with the organization of manuscript references. E.L. and S.B. provided the CVD-grown monolayer graphene used in the experiments. H.J. and T.L. provided discussions and insights on the interpretation of the molecular transport mechanisms. All authors discussed the results and contributed to the final version of the manuscript.

Notes

The authors declare no competing financial interest.

ACKNOWLEDGMENTS

This work was supported by the National R&D Program through the National Research Foundation of Korea (NRF) grant funded by the Korea government (MSIT) (no. RS-2023-00220077, RS-2024-00407271, RS-2024-00439520, RS-2025-00520264, RS-2024-00451891, 2E33811-25-077, RS-2025-00557748) and the KU-KIST Graduate School Program of Korea University, and a Korea University Future Research Grant.

REFERENCES

(1) Carroll, R. L.; Gorman, C. B. The Genesis of Molecular Electronics. *Angew. Chem., Int. Ed.* **2002**, *41*, 4378−4400.
(2) Chen, J.; Reed, M.; Rawlett, A.; Tour, J. Large On-Off Ratios and Negative Differential Resistance in a Molecular Electronic Device. *Science* **1999**, *286*, 1550−1552.
(3) Fiori, G.; Bonaccorso, F.; Iannaccone, G.; Palacios, T.; Neumaier, D.; Seabaugh, A.; Banerjee, S. K.; Colombo, L. Electronics Based on Two-Dimensional Materials. *Nat. Nanotechnol.* **2014**, *9*, 768−779.
(4) Wang, S.; Liu, X.; Zhou, P. The Road for 2D Semiconductors in the Silicon Age. *Adv. Mater.* **2022**, *34*, 2106886.
(5) Geim, A. K.; Grigorieva, I. V. Van der Waals Heterostructures. *Nature* **2013**, *499*, 419−425.
(6) Xia, F.; Wang, H.; Xiao, D.; Dubey, M.; Ramasubramaniam, A. Two-Dimensional Material Nanophotonics. *Nat. Photonics* **2014**, *8*, 899−907.
(7) Yang, Z.; Cazade, P.-A.; Lin, J.-L.; Cao, Z.; Chen, N.; Zhang, D.; Duan, L.; Nijhuis, C. A.; Thompson, D.; Li, Y. High Performance Mechano-Optoelectronic Molecular Switch. *Nat. Commun.* **2023**, *14*, 5639.
(8) Zhang, Y.; Liu, L.; Tu, B.; Cui, B.; Guo, J.; Zhao, X.; Wang, J.; Yan, Y. An Artificial Synapse Based on Molecular Junctions. *Nat. Commun.* **2023**, *14*, 247.
(9) Jang, J.; Kim, J.-K.; Shin, J.; Kim, J.; Baek, K.-Y.; Park, J.; Park, S.; Kim, Y. D.; Parkin, S. S.; Kang, K.; et al. Reduced Dopant-Induced Scattering in Remote Charge-Transfer-Doped MoS_2 Field-Effect Transistors. *Sci. Adv.* **2022**, *8*, No. eabn3181.
(10) Sim, D. M.; Kim, M.; Yim, S.; Choi, M.-J.; Choi, J.; Yoo, S.; Jung, Y. S. Controlled Doping of Vacancy-Containing Few-Layer MoS_2 via Highly Stable Thiol-Based Molecular Chemisorption. *ACS Nano* **2015**, *9*, 12115−12123.
(11) Reed, M. A.; Zhou, C.; Muller, C.; Burgin, T.; Tour, J. Conductance of a Molecular Junction. *Science* **1997**, *278*, 252−254.
(12) Song, H.; Kim, Y.; Jang, Y. H.; Jeong, H.; Reed, M. A.; Lee, T. Observation of Molecular Orbital Gating. *Nature* **2009**, *462*, 1039−1043.
(13) Li, Y.; Buerkle, M.; Li, G.; Rostamian, A.; Wang, H.; Wang, Z.; Bowler, D. R.; Miyazaki, T.; Xiang, L.; Asai, Y.; et al. Gate Controlling of Quantum Interference and Direct Observation of Anti-Resonances in Single Molecule Charge Transport. *Nat. Mater.* **2019**, *18*, 357−363.
(14) Shin, J.; Yang, S.; Jang, Y.; Eo, J. S.; Kim, T.-W.; Lee, T.; Lee, C.-H.; Wang, G. Tunable Rectification in a Molecular Heterojunction with Two-Dimensional Semiconductors. *Nat. Commun.* **2020**, *11*, 1412.
(15) Jariwala, D.; Marks, T. J.; Hersam, M. C. Mixed-Dimensional van der Waals Heterostructures. *Nat. Mater.* **2017**, *16*, 170−181.
(16) Schwierz, F. Graphene Transistors. *Nat. Nanotechnol.* **2010**, *5*, 487−496.
(17) Kanungo, S.; Ahmad, G.; Sahatiya, P.; Mukhopadhyay, A.; Chattopadhyay, S. 2D materials-based nanoscale tunneling field effect transistors: current developments and future prospects. *Npj 2D Mater. Appl.* **2022**, *6*, 83.
(18) Gao, F.; Yang, H.; Hu, P. Interfacial Engineering for Fabricating High-Performance Field-Effect Transistors Based on 2D Materials. *Small Methods* **2018**, *2*, 1700384.
(19) Park, H.; Park, J.; Lim, A. K.; Anderson, E. H.; Alivisatos, A. P.; McEuen, P. L. Nanomechanical Oscillations in a Single-C_{60} Transistor. *Nature* **2000**, *407*, 57−60.
(20) Guo, X.; Small, J. P.; Klare, J. E.; Wang, Y.; Purewal, M. S.; Tam, I. W.; Hong, B. H.; Caldwell, R.; Huang, L.; O'Brien, S.; et al. Covalently Bridging Gaps in Single-Walled Carbon Nanotubes with Conducting Molecules. *Science* **2006**, *311*, 356−359.
(21) Yan, C.; Fang, C.; Gan, J.; Wang, J.; Zhao, X.; Wang, X.; Li, J.; Zhang, Y.; Liu, H.; Li, X.; et al. From Molecular Electronics to Molecular Intelligence. *ACS Nano* **2024**, *18*, 28531−28556.
(22) Richter, S.; Mentovich, E.; Elnathan, R. Realization of Molecular-Based Transistors. *Adv. Mater.* **2018**, *30*, 1706941.
(23) Cui, A.; Dong, H.; Hu, W. Nanogap Electrodes towards Solid State Single-Molecule Transistors. *Small* **2015**, *11*, 6115−6141.
(24) Jia, C.; Famili, M.; Carlotti, M.; Liu, Y.; Wang, P.; Grace, I. M.; Feng, Z.; Wang, Y.; Zhao, Z.; Ding, M. Quantum Interference Mediated Vertical Molecular Tunneling Transistors. *Sci. Adv.* **2018**, *4*, No. eaat8237.
(25) Kim, D.; Lee, H.; Song, M.; Nam, J.; Lee, C.; Woo, J.; Jang, J.; Jeong, M.; Yeo, H.; Lee, R.-G.; et al. Enhanced Gating Efficiency in Vertical Mixed Molecular Transistors with Deep Orbital Level. *Sci. Adv.* **2025**, *11*, No. eadt3603.
(26) McCreery, R. L.; Bergren, A. J. Progress with Molecular Electronic Junctions: Meeting Experimental Challenges in Design and Fabrication. *Adv. Mater.* **2009**, *21*, 4303−4322.
(27) Jia, C.; Guo, X. Molecule−Electrode Interfaces in Molecular Electronic Devices. *Chem. Soc. Rev.* **2013**, *42*, 5642−5660.
(28) Chua, L.-L.; Zaumseil, J.; Chang, J.-F.; Ou, E. C.-W.; Ho, P. K.-H.; Sirringhaus, H.; Friend, R. H. General Observation of n-Type Field-Effect Behaviour in Organic Semiconductors. *Nature* **2005**, *434*, 194−199.

(29) Yoon, M.-H.; Kim, C.; Facchetti, A.; Marks, T. J. Gate Dielectric Chemical Structure−Organic Field-Effect Transistor Performance Correlations for Electron, Hole, and Ambipolar Organic Semiconductors. *J. Am. Chem. Soc.* **2006**, *128*, 12851−12869.
(30) Wang, Z.; Li, Z.; Li, C.; Ji, X.; Song, X.; Yu, X.; Wang, L.; Hu, W. Generic Dynamic Molecular Devices by Quantitative Non-Steady-State Proton/Water-Coupled Electron Transport Kinetics. *Proc. Natl. Acad. Sci. U. S. A.* **2023**, *120*, No. e2304506120.
(31) Wang, Y.; Zhang, Q.; Astier, H.P.; Nickle, C.; Soni, S.; Alami, F.A.; Borrini, A.; Zhang, Z.; Honnigfort, C.; Braunschweig, B.; et al. Dynamic Molecular Switches with Hysteretic Negative Differential Conductance Emulating Synaptic Behaviour. *Nat. Mater.* **2022**, *21*, 1403−1411.
(32) Wang, Y.; Zhang, Q.; Nickle, C.; Zhang, Z.; Leoncini, A.; Qi, D. C.; Borrini, A.; Han, Y.; Del Barco, E.; Thompson, D.; et al. Molecular-Scale In-Operando Reconfigurable Electronic Hardware. *Nanoscale Horiz.* **2025**, *10*, 349−358.
(33) Weiss, E. A.; Kaufman, G. K.; Kriebel, J. K.; Li, Z.; Schalek, R.; Whitesides, G. M. Si/SiO_2-Templated Formation of Ultraflat Metal Surfaces on Glass, Polymer, and Solder Supports: Their Use as Substrates for Self-Assembled Monolayers. *Langmuir* **2007**, *23*, 9686−9694.
(34) Karuppannan, S. K.; Hongting, H.; Troadec, C.; Vilan, A.; Nijhuis, C. A. Ultrasmooth and Photoresist-Free Micropore-Based EGaIn Molecular Junctions: Fabrication and How Roughness Determines Voltage Response. *Adv. Funct. Mater.* **2019**, *29*, 1904452.
(35) Krabbenborg, S. O.; Wilbers, J. G.; Huskens, J.; van der Wiel, W. G. Symmetric Large-Area Metal-Molecular Monolayer-Metal Junctions by Wedging Transfer. *Adv. Funct. Mater.* **2013**, *23*, 770−776.
(36) Ham, S.; Jang, J.; Koo, D.; Gi, S.; Kim, D.; Jang, S.; Kim, N. D.; Bae, S.; Lee, B.; Lee, C.-H.; Wang, G. Artificial Neuromodulator−Synapse Mimicked by a Three-Terminal Vertical Organic Ferroelectric Barristor for Fast and Energy-Efficient Neuromorphic Computing. *Nano Energy* **2024**, *124*, 109435.
(37) Kim, S.; Dong, Y.; Hossain, M. M.; Gorman, S.; Towfeeq, I.; Gajula, D.; Childress, A.; Rao, A. M.; Koley, G. Piezoresistive Graphene/P(VDF-TrFE) Heterostructure Based Highly Sensitive and Flexible Pressure Sensor. *ACS Appl. Mater. Interfaces* **2019**, *11*, 16006−16017.
(38) Hassanpour Amiri, M.; Heidler, J.; Müllen, K.; Asadi, K. Design Rules for Memories Based on Graphene Ferroelectric Field-Effect Transistors. *ACS Appl. Electron. Mater.* **2020**, *2*, 2−8.
(39) Kim, K. L.; Lee, W.; Hwang, S. K.; Joo, S. H.; Cho, S. M.; Song, G.; Cho, S. H.; Jeong, B.; Hwang, I.; Ahn, J.-H. Epitaxial Growth of Thin Ferroelectric Polymer Films on Graphene Layer for Fully Transparent and Flexible Nonvolatile Memory. *Nano Lett.* **2016**, *16*, 334−340.
(40) Meng, N.; Zhu, X.; Mao, R.; Reece, M. J.; Bilotti, E. Nanoscale Interfacial Electroactivity in PVDF/PVDF-TrFE Blended Films with Enhanced Dielectric and Ferroelectric Properties. *J. Mater. Chem. C* **2017**, *5*, 3296−3305.
(41) Seo, J.; Son, J. Y.; Kim, W.-H. Structural and Ferroelectric Properties of P(VDF-TrFE) Thin Films Depending on the Annealing Temperature. *Mater. Lett.* **2019**, *238*, 294−297.
(42) Naud, C.; Calas, P.; Commeyras, A. Critical Influence of the Fluorinated Chain Length in the Self-Assembly of Terminally Perfluorinated Alkanethiol Monolayers on Gold Surfaces. An Electrochemical Study. *Langmuir* **2001**, *17*, 4851−4857.
(43) Kobayashi, S.; Nishikawa, T.; Takenobu, T.; Mori, S.; Shimoda, T.; Mitani, T.; Shimotani, H.; Yoshimoto, N.; Ogawa, S.; Iwasa, Y. Control of Carrier Density by Self-Assembled Monolayers in Organic Field-Effect Transistors. *Nat. Mater.* **2004**, *3*, 317−322.
(44) Tamada, K.; Ishida, T.; Knoll, W.; Fukushima, H.; Colorado, R.; Graupe, M.; Shmakova, O.; Lee, T. Molecular Packing of Semifluorinated Alkanethiol Self-Assembled Monolayers on Gold: Influence of Alkyl Spacer Length. *Langmuir* **2001**, *17*, 1913−1921.
(45) Eo, J. S.; Shin, J.; Yang, S.; Jeon, T.; Lee, J.; Choi, S.; Lee, C. H.; Wang, G. Tailoring the Interfacial Band Offset by the Molecular Dipole Orientation for a Molecular Heterojunction Selector. *Adv. Sci.* **2021**, *8*, 2101390.
(46) De Boer, B.; Hadipour, A.; Mandoc, M. M.; Van Woudenbergh, T.; Blom, P. W. Tuning of Metal Work Functions with Self-Assembled Monolayers. *Adv. Mater.* **2005**, *17*, 621−625.
(47) Seo, S.; Min, M.; Lee, J.; Lee, T.; Choi, S. Y.; Lee, H. Solution-Processed Reduced Graphene Oxide Films as Electronic Contacts for Molecular Monolayer Junctions. *Angew. Chem., Int. Ed.* **2012**, *51*, 108−112.
(48) Engelkes, V. B.; Beebe, J. M.; Frisbie, C. D. Length-Dependent Transport in Molecular Junctions Based on SAMs of Alkanethiols and Alkanedithiols: Effect of Metal Work Function and Applied Bias on Tunneling Efficiency and Contact Resistance. *J. Am. Chem. Soc.* **2004**, *126*, 14287−14296.
(49) Eo, J. S.; Shin, J.; Jeon, T.; Jang, J.; Wang, G. Tilt-Engineered Molecular-Scale Selector for Enhanced Learning in Artificial Neural Networks. *Adv. Funct. Mater.* **2024**, *34*, 2311103.
(50) Wang, W.; Lee, T.; Reed, M. A. Mechanism of Electron Conduction in Self-Assembled Alkanethiol Monolayer Devices. *Phys. Rev. B* **2003**, *68*, 035416.
(51) Chen, Y.; Jia, Y.; Chen, Y.; Shi, Z.; Lv, S.; Jiang, K.; Liu, M.; Wu, T.; Li, D.; Sun, X. Infrared Light Rewritable Optoelectronic Memories in Graphene-P(VDF-TrFE) Ferroelectric Field-Effect Transistor. *ACS Appl. Electron. Mater.* **2024**, *6*, 4336−4344.
(52) Bazzari, A. H.; Parri, H. R. Neuromodulators and Long-Term Synaptic Plasticity in Learning and Memory: A Steered-Glutamatergic Perspective. *Brain Sci.* **2019**, *9*, 300.
(53) Shen, C.-K.; Chaurasiya, R.; Chen, K.-T.; Chen, J.-S. Synaptic Emulation via Ferroelectric P(VDF-TrFE) Reinforced Charge Trapping/Detrapping in Zinc−Tin Oxide Transistor. *ACS Appl. Mater. Interfaces* **2022**, *14*, 16939−16948.
(54) Xie, P.; Huang, Y.; Wang, W.; Meng, Y.; Lai, Z.; Wang, F.; Yip, S.; Bu, X.; Wang, W.; Li, D.; et al. Ferroelectric P(VDF-TrFE) Wrapped InGaAs Nanowires for Ultralow-Power Artificial Synapses. *Nano Energy* **2022**, *91*, 106654.
(55) Udaya Mohanan, K.; Cho, S.; Park, B.-G. Optimization of the Structural Complexity of Artificial Neural Network for Hardware-Driven Neuromorphic Computing Application. *Appl. Intell.* **2023**, *53*, 6288−6306.
(56) Xu, Z.; Ni, Y.; Sun, M.; Yuan, Y.; Wu, N.; Xu, W. Graphene/F16CuPc Synaptic Transistor for the Emulation of Multiplexed Neurotransmission. *J. Semicond.* **2025**, *46*, 012603.
(57) Erb, R. J. Introduction to Backpropagation Neural Network Computation. *Pharm. Res.* **1993**, *10*, 165−170.
(58) Wythoff, B. J. Backpropagation Neural Networks: A Tutorial. *Chemom. Intell. Lab. Syst.* **1993**, *18*, 115−155.
(59) Horowitz, M. 1.1 Computing's Energy Problem (and What We Can Do about It). In *Proceedings of the IEEE International Solid-State Circuits Conference (ISSCC)*; IEEE, 2014; pp 10−14.

https://doi.org/10.1021/acsnano.5c16879
ACS Nano 2025, 19, 41386−41395